PHYSICAL REVIEW B VOLUME 47, NUMBER 14 1 APRIL 1993-II

# Short-range cation ordering in $Li_xNi_{2-x}O_2$

Jan N. Reimers, W. Li, and J. R. Dahn
*Department of Physics, Simon Fraser University, Burnaby, British Columbia, Canada V5A 1S6*

(Received 21 October 1992)

The series $Li_xNi_{2-x}O_2$ undergoes a structural phase transition near $x_c=0.62$, from cubic ($x<0.62$) to hexagonal symmetry ($x>0.62$). The transition is driven by ordering of the cations into layers of Li and Ni, which are perpendicular to one of the cubic $\langle 111 \rangle$ directions. Here we report synchrotron x-ray data for 18 samples with compositions in the range $0.2 \le x \le 1.0$. The degree of cation ordering for samples near the critical composition was found to be sensitive to the annealing rate used during sample preparation. Quantitative estimates for the coherence lengths of short- and long-range-ordered domains are extracted from the data. The order parameter and cell constants are also determined as a function of composition $x$. Some implications of the domain structure on interpretation of electronic properties and magnetic ordering are briefly discussed.

## INTRODUCTION

NiO and $LiNiO_2$ are end members of the series $Li_xNi_{2-x}O_2$. NiO crystallizes with the cubic rock-salt structure. $LiNiO_2$ is hexagonal and has the same close-packed oxygen network as NiO but with alternating basal planes of Li and Ni atoms, as shown in Fig. 1. The basal planes in the hexagonal structure correspond to cubic (111) planes of NiO. Near $x=0.62$ there is an apparently continuous transition[1-3] from the cubic symmetry of NiO to the hexagonal symmetry of $LiNiO_2$. The series $Li_xNi_{2-x}O_2$ has recently been characterized using Rietveld x-ray profile analysis and modeled as a lattice gas using empirically determined cation-cation interactions.[4] The critical composition $x_c=0.62(1)$, where the system transforms from cubic to hexagonal symmetry, was also determined.

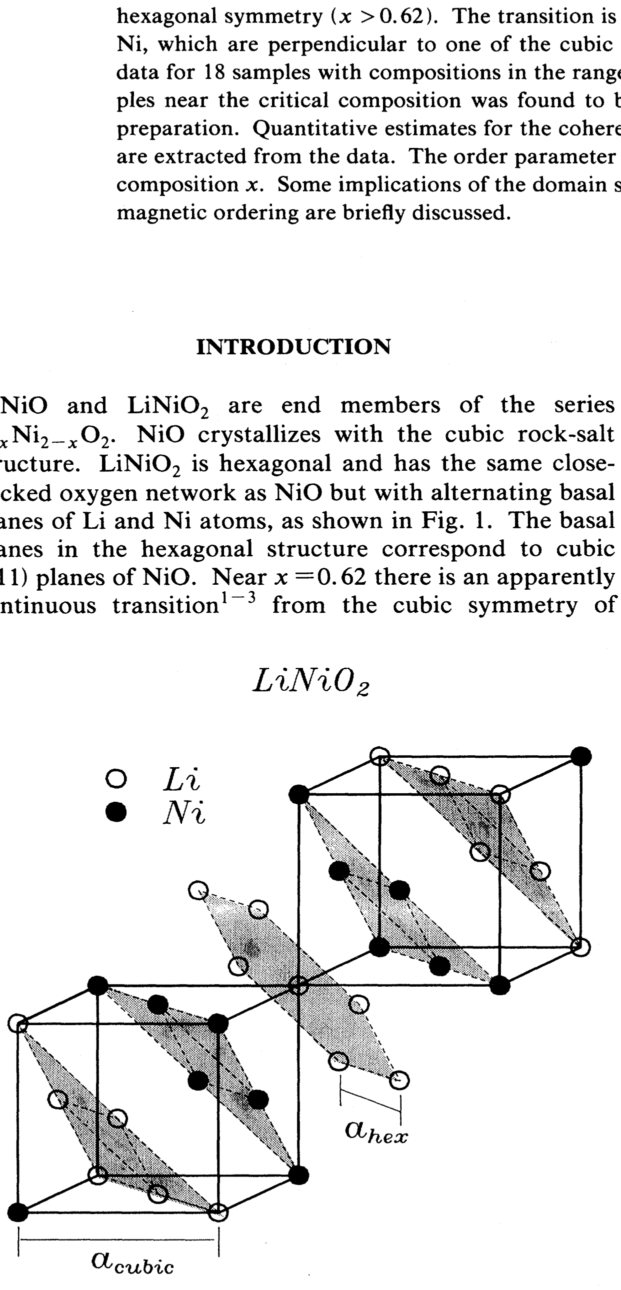

FIG. 1. Schematic representation of the layered cation structure of $LiNiO_2$, oxygen atoms are not shown. The solid lines outline two unit cells of the underlying cubic NiO structure obtained by replacing all Li atoms with Ni. The hexagonal and cubic cell edges are indicated and the hexagonal $c$ axis corresponds to the body diagonal through both cubic unit cells (not shown).

NiO is a prototypical Mott-Hubbard insulator[5] whose electronic structure has been the subject of intense interest for many years.[5,6] In a naive ionic picture of $Li_xNi_{2-x}O_2$, introduction of Li results in the oxidation of $Ni^{2+}$ to $Ni^{3+}$, i.e., electron holes will reside on Ni. Interpretation of the bulk magnetic properties were based on this assumption.[1] However, recent x-ray absorption spectroscopy (XAS),[7] x-ray photoemission spectroscopy (XPS),[8] and photoemission[9] studies suggest that the holes are of O $2p$ character rather than Ni $3d$. Hartree-Fock molecular cluster calculations support this result.[10] Based on bulk susceptibility and resistivity measurements, Dutta *et al.*[11] have argued that the holes introduced by oxidation of $Li_xNi_{2-x}O_2$ ($x=0.96$ and 0.92) do not occupy O $2p$ bands. They also suggest that, upon oxidation, the ionic model breaks down due to very strong Ni-O covalent bonding.

For $x \approx 1$, $Li_xNi_{2-x}O_2$ is of considerable interest because of its ability to reversibly intercalate lithium. High-density energy storage can be achieved using $LiNiO_2$ as an electrode material in advanced lithium batteries.[12] The performance of the cells depends on the stoichiometry. As $x$ in $Li_xNi_{2-x}O_2$ deviates from 1, Ni atoms occupy sites in the lithium layers and presumably impede the diffusion of Li. The optical properties of $Li_xNi_{2-x}O_2$ are also of interest because of its possible application as an electrochromic material.[13]

Due to the scientific and technological importance of this class of materials we feel it is important to characterize the structural properties of $Li_xNi_{2-x}O_2$ carefully. The long-range-ordered crystal structures of the whole series $Li_xNi_{2-x}O_2$ ($0.2 \le x \le 1.0$) have been reported previously. Here we focus on a quantitative characterization of the short-range correlations that exist between the cations over a wide range in composition, $0.2 \leq x \leq 0.8$. The improved resolution of the synchrotron x-ray data allow a definitive separation of the long-range-ordered (LRO) and short-range-ordered (SRO) components of the superlattice reflections. For $x > 0.3$, broad superlattice reflections are observed, resulting from a tendency of the Li and Ni atoms to order locally in alternating (111) planes of the cubic NiO lattice. From superlattice peak widths and integrated intensities we determine quantitative estimates for the coherent domain sizes and the degree of cation ordering, as $x$ varies.

## EXPERIMENT

To our knowledge $Li_xNi_{2-x}O_2$ can only be made in powder form. Samples were prepared by reacting stoichiometric mixtures of $LiOH \cdot H_2O$ and $Ni(OH)_2$. The powders were ground and heated at 700 °C for 2 h in air, followed by slow cooling over several hours to room temperature. Some of the samples in this study are the same samples used in Ref. 4. Both annealed (cooled uniformly for 18 h from 700–100 °C) and quenched samples were prepared by refiring samples with compositions near the critical composition, $x_c$. All samples were initially characterized by Rietveld profile fitting of Cu$K_\alpha$ x-ray-diffraction data, yielding cell constants and measured stoichiometries, $x_{\text{meas}}$. At this stage of the analysis any regions of diffuse scattering arising from SRO in samples near $x_c$ were excluded from the profile fit. We found that $x_{\text{meas}}$ was for the most part larger than $x$ determined from the mole ratios of the starting materials. Details can be found in Ref. 4. Throughout this work we will employ the measured values of $x$, $x_{\text{meas}}$, exclusively.

In house x-ray-diffraction measurements were made using a Phillips powder diffractometer with a diffracted beam monochromator and a copper target x-ray tube. Rietveld profile refinements were carried out using the Hill and Howard[14] package to determine stoichiometries, $x$, and cell constants. Synchrotron x-ray data were obtained from beam line X7A at the National Synchrotron Light Source (NSLS) at Brookhaven National Laboratories (BNL). Bending magnet radiation was monochromated using a double crystal Ge(111) monochromator. Effective powder averaging was achieved by rocking the sample angle, $\theta$, for each data point. The wavelength, $\lambda = 1.5046$ Å, and the resolution half-width, $2\theta_{\text{res}} = 0.070(5)°$, were determined using a well-crystallized sample of CeO. No scattered beam analyzer was used. All intensities were normalized by the count rates from an incident beam monitor detector.

## RESULTS AND DISCUSSION

Throughout this work Miller indices referring to the cubic unit cell will be labeled with a subscript $C$, and those referring the hexagonal unit cell will be labeled with a subscript $H$. The cubic NiO structure exhibits three Bragg reflections $(111)_C$, $(200)_C$, and $(220)_C$, in the $2\theta$ range considered. Cation ordering into alternating layers of Li and Ni results in some scattered intensity at the superlattice reflections $(\frac{1}{2},\frac{1}{2},\frac{1}{2})_C$ and $(\frac{1}{2},\frac{1}{2},\frac{3}{2})_C$. The $(\frac{1}{2},\frac{1}{2},\frac{1}{2})_C$, $(\frac{1}{2},\frac{1}{2},\frac{3}{2})_C$, and $(200)_C$ cubic reflections correspond, respectively, in the hexagonal representation, to $(003)_H$, $(101)_H$, and $(104)_H$. The $(111)_C$ and $(220)_C$ cubic reflections split in the hexagonal metric as follows:

$$(111)_C \rightarrow (006)_H + (102)_H \, ,$$

$$(220)_C \rightarrow (108)_H + (110)_H \, .$$

This is seen in Fig. 2 where measured spectra are shown for two stoichiometries, $x = 0.331$ [cubic, Fig. 2(a)] and $x = 1.01$ [hexagonal, Fig. 2(b)]. Throughout we will refer to $(102)_H$, $(006)_H$, $(104)_H$, $(108)_H$, and $(110)_H$ as the principle reflections because they also occur in the cubic phase. The structure factors for the principle reflections are insensitive to the degree of cation ordering. Correspondingly the $(003)_H$ and $(101)_H$ reflections will be referred to as the superlattice reflections.

To extract quantitative information we have least-squares fit the data for all measured reflections simultaneously. A sloping background function was used. Peak shapes were modeled with a Pseudo-Voigt peak shape

$$I(2\theta) = \gamma \frac{w/\pi}{w^2 + (2\theta - 2\theta_0)^2} + (1-\gamma)\left[\frac{\ln 2}{\pi}\right]^{1/2} \frac{1}{w} \exp\left[\frac{\ln 2 (2\theta - 2\theta_0)^2}{w^2}\right] , \qquad (1)$$

which is a mixture of normalized Lorentzian and Gaussian components. Here, $2\theta_0$ is the peak center, $w$ is the peak *half* width at half maximum, and $\gamma$ is the Lorentzian-Gaussian mixing parameter. For the principle reflections which were close to resolution limited the peak shape was allowed to vary as a function of scattering angle

$$\gamma = \gamma_0 + \gamma_1 2\theta \, , \qquad (2)$$

where $\gamma_0$ and $\gamma_1$ are refinable parameters. Peak shapes

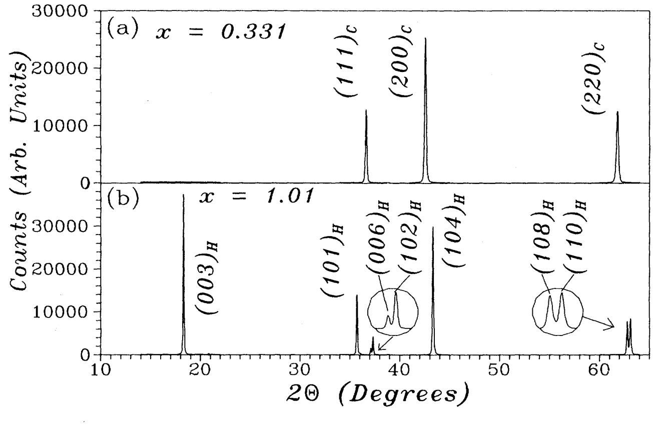

FIG. 2. Sample x-ray-diffraction patterns for cubic ($x = 0.331$) and hexagonal ($x = 1.01$) $Li_xNi_{2-x}O_2$. All reflections are labeled with respect to the appropriate unit cell.

for SRO and LRO superlattice reflections were fixed to be pure Lorentzian, $\gamma = 1$. Peak widths were calculated as the sum of a constant resolution component and a Sherrer[15] term which takes the average coherence length in the sample into account:

$$2w = 2\theta_{\rm res} + \frac{\lambda}{\xi \cos\theta} . \qquad (3)$$

$2\theta_{\rm res} \approx 0.070(5)^\circ$ and $0.14(3)^\circ$ are the estimated resolution half-widths for synchrotron and in-house instruments, respectively. $\xi$ is the coherence length in Å.

Three coherence lengths were refined. The width of the principle reflections determined the average particle size, $\xi_{\rm PS}$. For $x \geq 0.5$ the superlattice reflections were modeled with two coherence lengths, $\xi_{\rm SRO}$ and $\xi_{\rm LRO}$, corresponding to the short-range- and long-range-ordered components, respectively. For $x < x_c$ only the SRO component was included except in one case to be discussed below. The same coherence lengths were used for both of the superlattice reflections. The width of the $(003)_H$ reflection depends solely on the longitudinal correlation length along the hexagonal $c$ direction, as the transverse width of this reflection is integrated over in the powder average. The interpretation of the $(101)_H$ width is, in general, not as simple because finite distance transverse correlations will also contribute to the width of this peak. However, we saw little evidence in our data that the transverse and longitudinal correlations are significantly different. The calculated intensities were also scaled by the Lorentz-polarization (LP) factor for peak *profiles*:

$$\mathrm{LP}_{\rm prof}(2\theta) = \frac{1 - p + p\cos^2 2\theta}{\sin\theta \sin\theta_0} , \qquad (4)$$

where $p \approx 0.05$ (Ref. 16) is the degree of polarization for the synchrotron in the horizontal plane and $2\theta_0$ is the Bragg angle of the peak. The derivation of the Lorentz factor in (4), $1/(\sin\theta \sin\theta_0)$, is described in the Appendix. The LP correction will slightly increase the calculated intensity on the low angle side of the $(003)_H$ reflection, when it is broad.

Peak positions were determined from the cell constants, $a$ and $c$,

$$2\sin[\theta_0(hkl)_H]/\lambda = [\tfrac{4}{3}(h^2 + hk + k^2)/a^2 + l^2/c^2]^{1/2} . \qquad (5)$$

In the cubic phase, $a$ was refined and the ratio $\sqrt{24}a/c = 1$ was fixed. In the hexagonal phase $\sqrt{24}a/c$ was also allowed to vary.

Three sample fits are shown in Fig. 3 for $x = 0.331$ [Fig. 3(a)], 0.670 [Fig. 3(b)], and 0.874 [Fig. 3(c)]. For $x = 0.331$ one observes very weak scattering at the $(003)_H$ reflection ($2\theta \approx 18^\circ$) indicating a small degree of cation ordering. The coherence length $\xi_{\rm SRO} = 17(1)$ Å corresponds to about seven cation layers. Error bars that we report are statistical values obtained from the least-squares fit and are therefore underestimated. There is no evidence for superlattice scattering at the $(101)_H$ scattering angle ($2\theta \approx 35.3^\circ$). For $x = 0.670$ both the $(003)_H$ and $(101)_H$ reflections are clearly seen. This is very near and just above the estimated critical composition, $x_c = 0.62(1)$, therefore both LRO and SRO components are present. The LRO can occur with cation planes perpendicular to any of the four independent $\langle 111 \rangle_C$ directions, $(111)_C$, $(\bar{1}\bar{1}1)_C$, $(\bar{1}1\bar{1})_C$, or $(1\bar{1}\bar{1})_C$, with equal probability. Thus, as usual, spontaneous symmetry breaking occurs at the critical point. The SRO scattering above $x_c$ arises from small antiphase domains within a

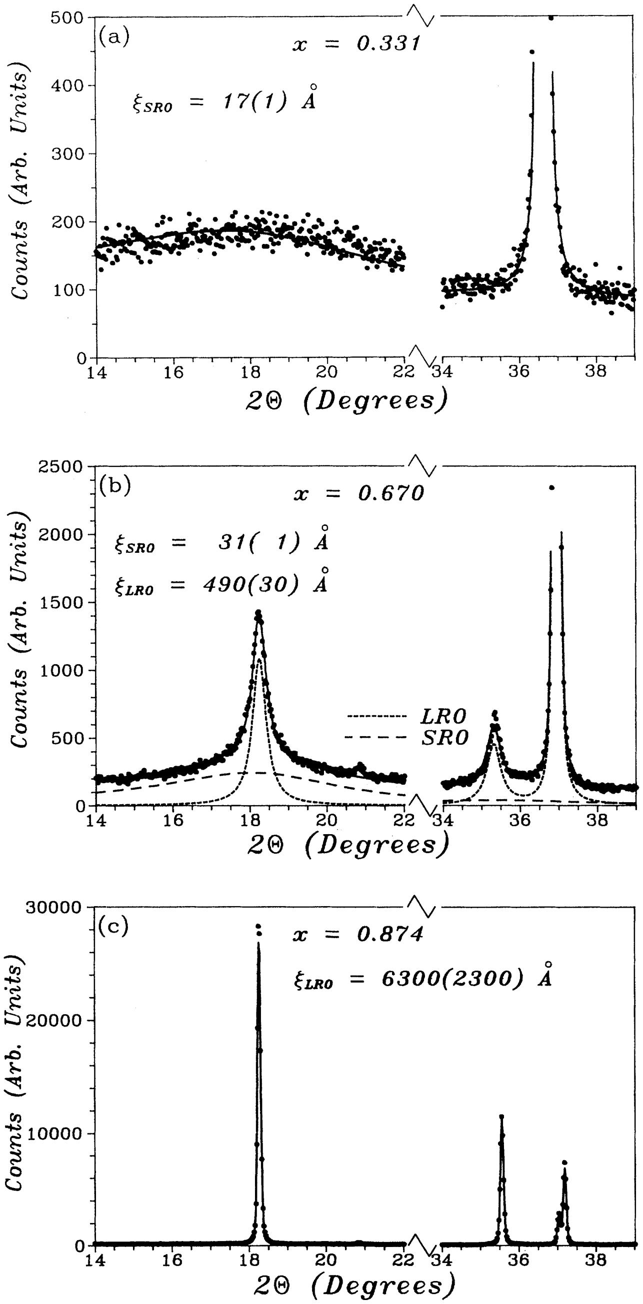

FIG. 3. Sample fits to the superlattice reflections for $x = 0.331$ (a), 0.670 (b), and 0.874 (c). In (b) the sample composition is just above $x_c$ (this sample was annealed) and the fitted SRO and LRO components of the superlattice reflections are plotted individually with dashed lines.

LRO domain, or small domains of cation layers perpendicular to any of the other three $\langle 111 \rangle_C$ directions within a LRO domain. For this sample, $\xi_{\mathrm{LRO}}$ determined from the superlattice reflections is significantly smaller than the particle size $\xi_{\mathrm{PS}}$ determined by the principle reflections. This was found to be true for all samples near $x_c$ for $x \leq 0.75$. For $x = 0.874$ one sees all reflections are sharp and the constraint $\xi_{\mathrm{LRO}} = \xi_{\mathrm{PS}}$ was imposed for samples with $x > 0.75$. At $x = 0.874$, SRO scattering is essentially indistinguishable from the background. The $(006)_H$-$(102)_H$ splitting is also clearly seen at this composition.

For samples near the critical composition, $x_c$, it is not always clear whether or not to include both coherence lengths, $\xi_{\mathrm{SRO}}$ and $\xi_{\mathrm{LRO}}$, or just the SRO component. We found that even for one sample with composition, $x \leq x_c$, it was necessary to include two coherence lengths to model the peak shape properly. We show this in Fig. 4, where the two-coherence-length fit in Fig. 4(b) is clearly a better representation of the observed peak shape. The fitted parameters from the two-coherence-length fit were used in the subsequent analysis. We propose three possible explanations for this.

(1) The samples are not homogeneous, so that particles with $x < x_c$ and $x > x_c$ are simultaneously present in one sample. This would be consistent with the transition being first order. Alternatively, the samples may have particles with the same composition, but cooled too rapidly for the ordered phase to fully develop.

(2) The Lorentzian line shape is not correct for modeling the critical scattering near $x_c$.

(3) The previously determined value, $x_c = 0.62(1)$, is wrong.

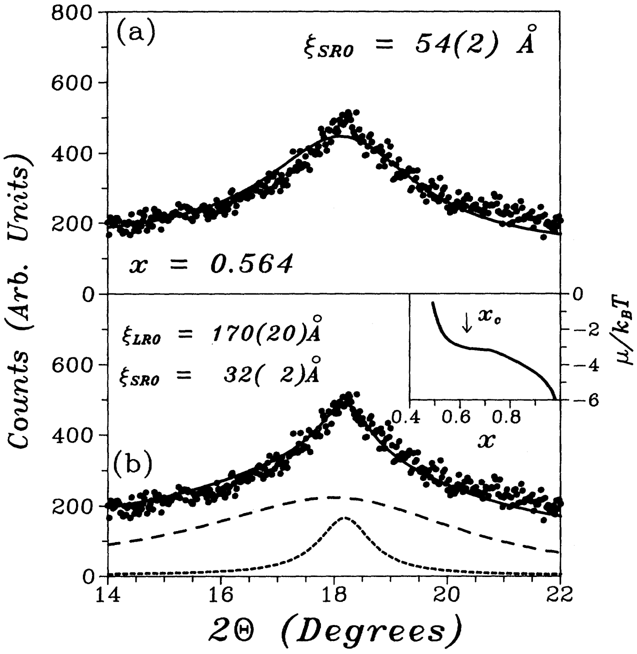

FIG. 4. Attempts to model the critical scattering at $(003)_H$ on an unannealed sample, with (a) one and (b) two coherence lengths, for sample composition $x = 0.564$, which is below the previously determined value of $x_c$. The two-coherence-length fit clearly gives a better representation of the observed peak shape. The inset shows the chemical potential difference between Ni and Li which is seen to be comparatively flat near the critical composition.

We suspect that explanation (1) is the most likely cause for the following reason. Near a phase transition the difference in chemical potentials between Ni and Li,

$$\mu = \mu^{\mathrm{Ni}} - \mu^{\mathrm{Li}} , \tag{6}$$

is only very weakly dependent on the composition, $x$. The inset in Fig. 4(b) shows this potential difference as calculated from a lattice gas model with appropriate interactions using the Monte Carlo method on a $12 \times 12 \times 12$ cubic unit-cell lattice. The details of this calculation can be found in Ref. 4. The weak composition dependence of $\mu$ is a general feature of lattice-gas phase transitions and is not specific to our model.[17] This means that near $x_c$ the cost in free energy of concentration gradients in the sample becomes small, thus making homogeneous sample preparation more difficult. This problem can only be solved by decreasing the cooling rate during sample preparation.

We have refired many of the samples with compositions near $x_c$ and annealed them slowly from 700 °C to 100 °C over a period of 18 h. Some samples were also quenched, for comparison, by quickly removing the samples from the furnace to room temperature. As an example we show the diffraction data near the $(003)_H$ reflection for the quenched [Fig. 5(a)] and slow cooled [Fig. 5(b)] sample with composition $x = 0.660$. The annealing process allowed the cations to order coherently over a length

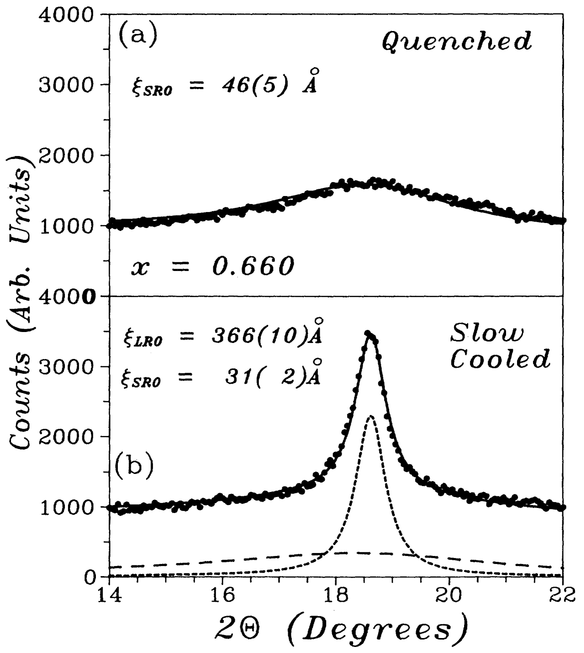

FIG. 5. Comparison of the scattering near the $(003)_H$ Bragg reflection for a (a) quenched sample and (b) a sample that was slow cooled for 18 h.

scale that is an order of magnitude larger than that of the quenched sample. In our analysis below we plot open circles for data from samples that were refired and annealed for 18 h. X-ray data for the annealed samples were measured in house which did not allow us to probe the larger length scales accessed by the synchrotron data. The sample which appeared to have some degree of long-range order (see Fig. 4) was also annealed for a period of 100 h and showed essentially no differences from the 18-h annealed sample with the same composition. This gives us some confidence that we are achieving equilibrium in the 18-h cooling time allowed for the annealed samples. Unless otherwise stated all subsequent discussion will apply to those data obtained from the annealed samples.

The SRO and LRO coherence lengths are shown on a logarithmic scale as function of composition in Fig. 6. We have only shown $\xi_{\mathrm{SRO}}$ for the unannealed samples (measured with synchrotron x-rays), the corresponding results for the annealed samples were very similar and are therefore not shown for clarity. $\xi_{\mathrm{SRO}}$ appears roughly symmetric about $x=\frac{1}{2}$. $\xi_{\mathrm{LRO}}$ shows a rapid increase from 100 Å at $x=0.55$ to over 2000 Å at $x=0.7$, at which point $\xi_{\mathrm{LRO}}$ became equivalent to the particle size, $\xi_{\mathrm{PS}}$. The error bars for the very large coherence lengths were primarily due to the uncertainty in the resolution width, $2\theta_{\mathrm{res}}$. The LRO coherence lengths for samples with compositions near $x_c$ are, in general, slightly larger than those of the unannealed samples but still much smaller than the observed particle sizes. The inset in Fig. 6 shows the average particle size $\xi_{\mathrm{PS}}$ on a logarithmic scale. There is considerable scatter in the particle size, with a general tendency towards larger particles as $x \rightarrow 1$. The range of particle sizes is most likely a result of subtle differences in grinding or firing of the starting materials. No significant correlations between the particle size and $\xi_{\mathrm{LRO}}$ are evident in the critical regime and hence we believe that our values of $\xi_{\mathrm{LRO}}$ are not adversely affected by inconsistencies in particle size as composition varies. Particle sizes for the annealed samples are again larger than the unannealed particles. Bragg peaks for the annealed samples were approaching the resolution limit of our laboratory instrument and hence there are large error bars for these data.

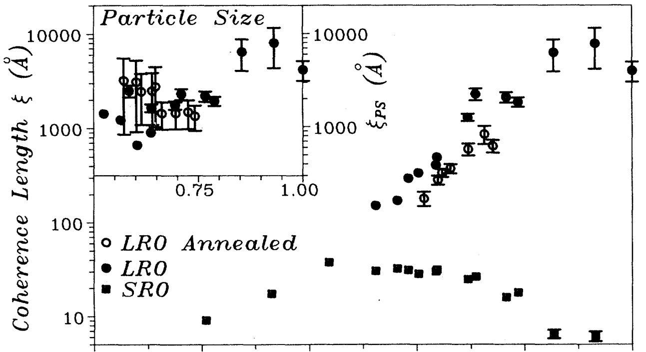

FIG. 6. LRO and SRO coherence lengths on a logarithmic scale for all compositions studied. The inset shows the measured particle sizes for all samples. Statistical error bars which are samller than the data point size are not shown.

Following Ref. 4, we can define an order parameter for the transition by labeling the predominantly Li-filled layers as $L$ layers, and the predominantly Ni filled layers as $N$ layers. The order parameter can then be defined as the difference in fractional Li (or Ni) occupations between the $L$ layers and the $N$ layers

$$\eta=|\langle x_L\rangle-\langle x_N\rangle| \ . \tag{7}$$

The order parameter is, to a very good approximation, proportional to the square root of the integrated intensity of superlattice reflections, $(003)_H$ and $(101)_H$. The superlattice intensities were divided by the measured $(104)_H$ intensity in order to get an absolute scale for each data set. Although the $(104)_H$ intensity is completely independent of the degree of cation ordering, it does depend on the composition, $x$, hence the normalized superlattice intensities were also corrected for this effect. Finally, the order parameters, $\eta(x)$, were calculated by fixing $\eta(1)=0.959$ as determined previously.[4] The annealed sample with the lowest nonzero value of $\eta$ was at composition $x=0.614$. Based on this we estimate $x_c=0.61(1)$ in good agreement with the previous result. The order parameter is shown in Fig. 7(a), where the solid line, which assumes $x_c=0.61$, is a guide to the eye. The data in Fig. 7(a) for the unannealed samples is rather poor compared to the annealed samples which show the expected sharp drop in $\eta(x)$ near $x_c$. We have only shown the SRO integrated intensities for the unannealed samples (measured with synchrotron x

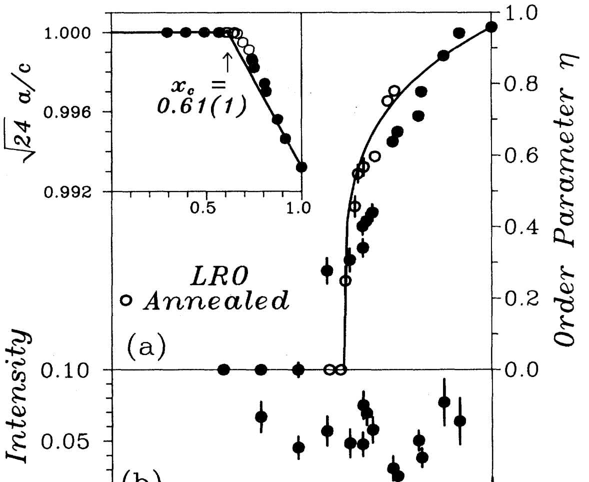

FIG. 7. (a) Order parameter for the cation ordering giving $x_c=0.61(1)$. The inset shows how the cell constant ratio $\sqrt{24}a/c$ deviates from 1 in the hexagonal phase. The solid line assumes $x_c=0.61$ and shows that the cell constants do not behave in a linear fashion above $x_c$. (b) Integrated intensity of the SRO scattering. Statistical error bars which are smaller than the data point size are not shown.

rays), the corresponding results for the annealed samples were very similar and are therefore not shown for clarity. The intensity of the SRO scattering is shown in Fig. 7(b), and is rather featureless.

The transition from cubic to hexagonal symmetry can also be studied by following the cell constant ratio $\sqrt{24}a/c$. This ratio is exactly 1 in the cubic phase and decreases from 1 above $x_c$, as the inset in Fig. 7(a) shows. For samples near $x_c$ we only show the results obtained from the annealed samples. The solid line here is a guide to the eye and shows that the ratio does not exhibit linear behavior just above $x_c$. We have recently discovered[18] that a cubic modified spinel structure of $LiCoO_2$ (i.e., $Li_2Co_2O_4$) is (a) very close in energy to the usual layered structure and (b) exhibits identical powder diffraction intensities to the layered structure. It is quite possible that this cubic phase also exists in $LiNiO_2$, particularly near $x_c$. This would explain the observed persistence of cubic cell constants ($\sqrt{24}a/c=1$) for compositions $x>x_c$. Earlier results in Ref. 4 were for unannealed samples and differ slightly. Samples with order parameters as large $\eta \approx 0.5$ still exhibit roughly cubic cell constants to within the resolution of our instrument.

## SUMMARY AND CONCLUSIONS

$Li_xNi_{2-x}O_2$ exhibits a phase transition from cubic to hexagonal symmetry at $x_c=0.62(1)$ which is driven by ordering of the cations into alternating $(111)_C$ layers. The samples near $x_c$ can be characterized by various types of order on three length scales: (1) $\xi_{PS}$ the average particle size for all compositions, (2) $\xi_{LRO}$, the coherence length of the cation LRO for $x>x_c$, and (3) $\xi_{SRO}$, the coherence length of the cation SRO for $x<x_c$, and of the cation SRO antiphase domains within the LRO domains for $x>x_c$.

The samples near the critical composition were found to require longer annealing times to equilibrate. This can be understood in terms of the cation chemical potential difference which is always insensitive to composition near a phase transition. This is an indirect cause of critical slowing down which is well known to occur at all critical points.

Future studies of the electronic structure and electrochemical properties in this series should take into consideration the partial cation ordering, especially for samples with compositions near $x_c$. For such samples the Ni valence states may be affected (i.e., apparent level broadening) by the distribution of environments that Ni sees. A similar argument applies to interpretation of O $2p$ bands. For compositions near $x_c$, O ions will commonly be coordinated by anywhere from 3 to 6 Ni ions. Also, nonlocal effects may be affected by the various length scales involved in the domain structure. For example, magnetic ordering will be impeded by the disorder of the Ni sublattice.

## ACKNOWLEDGMENTS

We would like to thank D. E. Cox for useful discussions and assistance with measurements. We acknowledge funding for a portion of this work, under the strategic grant program, from the Natural Sciences and Engineering Research Council of Canada (NSERC). Research carried out at the National Synchrotron Light Source, Brookhaven National Laboratory, was supported by the U.S. Department of Energy, Division of Materials Sciences and Division of Chemical Sciences.

## APPENDIX

It is common to analyze diffraction profiles in order to, for example, obtain information regarding particle size and lattice strain. Raw data are usually corrected[19] for effects such as polarization, Lorentz factor, and (in cases where the scatterer consists of one atom type) the atomic form factor. The Lorentz factor for *integrated* powder peak intensities is well known and described in most books on x-ray or neutron diffraction

$$L_{\text{int}}(2\theta)=\frac{1}{\sin^2\theta\cos\theta} . \tag{A1}$$

This form of the Lorentz factor has been incorrectly used in the past to correct diffraction line profiles. Yinghua has recently emphasized this point[20] and claims that for powder diffraction *profile* intensities the Lorentz factor is

$$L_{\text{prof}}(2\theta)=\frac{1}{\sin^2\theta} , \tag{A2}$$

where the factor of $\cos\theta$ in the denominator has been removed. This is the form originally derived by Friedel.[21] The difference between $L_{\text{int}}(2\theta)$ and $L_{\text{prof}}(2\theta)$ is only important at large scattering angles, $2\theta>90°$. Expression (A2) is valid for narrow peaks, but not for broad peaks (especially at low angles), as we shall show below. For example, in the extreme case of incoherent scattering where the scattering function $S(\mathbf{q})$ is a constant, one observes a constant background in the powder profile and not the $(\sin\theta)^{-2}$ dependence predicted by (A2). Below we will discuss powder averaging theory in detail and derive an exact expression for the powder average of any spherically symmetric scattering distribution, $S(\mathbf{q})$, centered at an arbitrary point in reciprocal space.

For a standard diffractometer arrangement (constant slit widths) the instrumental resolution function spans a constant volume in reciprocal space independent of the scattering angle $2\theta$. The scattering angle, $2\theta$, corresponds to all scattering wavevectors of magnitude, $q=2\sin\theta/\lambda$. The resolution function projected onto a sphere of radius $q$ defines a solid angle

$$\Omega=\frac{A}{4\pi q^2} , \tag{A3}$$

where $A$ is the area of the resolution function projection and is constant. This solid angle is directly proportional to the probability that a crystallite in the powder is correctly oriented for a scattering event characterized by wave vector $\mathbf{q}$. The factor $1/(4\pi q^2) \propto 1/\sin^2\theta$ in (A3) is sometimes referred to as the Lorentz factor,[22] however, we will show below that this is not, strictly speaking, correct.

To calculate the observed scattering at an angle $2\theta$ we must integrate over all scattering within a shell at $q=2\sin\theta/\lambda$ of thickness $dq$. We have

$$I(q)dq=\frac{A}{4\pi q^2}q^2dq\int d\Omega\, S(q,\Omega)\ , \tag{A4}$$

where the integral is over all angular coordinates of the scattering wave vector $\mathbf{q}$. To proceed further we must specify the scattering function to some extent. Of central importance is a scattering function with a peak centered at some arbitrary point in reciprocal space, $\mathbf{q}_0$,

$$S(\mathbf{q})=f(|\mathbf{q}-\mathbf{q}_0|^2)\ . \tag{A5}$$

Substituting (A5) into (A4) we obtain

$$\begin{aligned} I(q)dq&=\frac{Adq}{4\pi}2\pi\int_0^{\pi}d\alpha\,\sin\alpha f[q^2-2qq_0\cos(\alpha)+q_0^2]\\ &=\frac{Adq}{2}\frac{1}{2qq_0}\int_{(q-q_0)^2}^{(q+q_0)^2}dx\,f(x)\ , \qquad\qquad (A6)\\ I(q)&\propto\frac{1}{qq_0}\{g[(q+q_0)^2]-g[(q-q_0)^2]\}\ , \end{aligned}$$

where $g(x)=\int f(x)dx$. The factor $1/(qq_0)\propto 1/(\sin\theta\sin\theta_0)$ is the correct Lorentz factor for diffraction profiles which is valid for very broad peaks at low angles (arbitrary $q_0$) as well as narrow peaks. We see that the factor $1/q^2$ in (A3) is canceled by the factor of $q^2$ in shell volume [Eq. (A4)] and therefore should not be interpreted as the Lorentz factor.

As an example we apply this to the special but important case in which the scattering function is a normalized Gaussian of width $\varepsilon$:

$$S(\mathbf{q})=(\sqrt{\pi}\varepsilon)^{-3}\exp[-(\mathbf{q}-\mathbf{q}_0)^2/\varepsilon^2]\ , \tag{A7}$$

we obtain

$$\begin{aligned} I(q)\propto\frac{1}{qq_0\varepsilon}\{&\exp[-(q-q_0)^2/\varepsilon^2]\\ &-\exp[-(q+q_0)^2/\varepsilon^2]\}\ . \end{aligned} \tag{A8}$$

Hence the *exact* powder average of a Gaussian function is not a Gaussian. To make contact with conventional ideas we consider three limiting cases.

Case (1). $\varepsilon \ll q_0$. In this case the second term in parentheses in (A8) is completely negligible compared to the first and we are left with a Gaussian. Also, since $\varepsilon$ is very small (sharp peak) we can assume that $q$ is effectively constant across the width of the peak. This allows one to make approximation $q\approx q_0$ giving

$$I(q)\approx\frac{1}{q^2\varepsilon}\exp[-(q-q_0)^2/\varepsilon^2]\ . \tag{A9}$$

This expression has the approximate profile Lorentz factor (A2). However, we see no advantage in making the approximation $q\approx q_0$ as it introduces no simplifications for line-shape analysis.

Case (2). $\varepsilon < q_0$. In this case we assume $q_0$ is still large enough that the second term in parentheses in (A8) is negligible but that the peak is broad so that the approximation $q\approx q_0$ is no longer valid.

$$I(q)\approx\frac{1}{qq_0\varepsilon}\exp[-(q-q_0)^2/\varepsilon^2]\ . \tag{A10}$$

For broad peaks at a low angle the distinction between (A10) and (A9) becomes important. For analysis of diffraction peak profiles the data should be corrected for the factor $1/q$ in (A10) since $q_0$ is constant for any peak and not $1/q^2$ as suggested by (A2). Previous workers who used expressions like (A2) have actually introduced an artificial asymmetry into their line shapes.

Case (3). $\varepsilon \gg q_0$. In the asymptotic limit where $\varepsilon\rightarrow\infty$ one can show that (A8) approaches

$$I(q)\propto\varepsilon^{-3}+O(q^2/\varepsilon^5)\ , \tag{A11}$$

which corresponds to the constant background (with no Lorentz factor) expected for completely incoherent scattering. For this to work it is absolutely necessary to retain the second term in parentheses in (A8).

---

[1] J. B. Goodenough, D. G Wickham, and W. J. Croft, J. Phys. Chem. Solids **5**, 107 (1958); J. Appl. Phys. **29**, 382 (1958).

[2] V. W. Bronger, H. Bade, and W. Klemm, Z. Anorg. Allg. Chem. **333**, 188 (1964).

[3] I. J. Pickering, J. T. Lewandowski, A. J. Jacobson, and J. Goldstone, Solid State Ion. **53–56**, 405 (1992).

[4] W. Li, J. N. Reimers, and J. R. Dahn, Phys. Rev. B **46**, 3236 (1992).

[5] S. H. de Boer and E. J. W. Verwey, Proc. Phys. Soc. London, Sect. A **49**, 59 (1937); N. F. Mott, *ibid.* **62**, 416 (1949); J. Hubbard, Proc. R. Soc. London, Ser. A **276**, 238 (1963).

[6] K. Terakura, T. Oguchi, A. R. Williams, and J. Kübler, Phys. Rev. B **30**, 4734 (1984); J. Zaanen, G. A. Sawatzky, and J. W. Allen, J. Magn. Magn. Mater. **54-57**, 607 (1986); Z.-X. Shen, C. K. Shih, O. Jepsen, W. E. Spicer, I. Lindau, and J. W. Allen, Phys. Rev. Lett. **64**, 2442 (1990); D. D. Sarma, J. Solid State Chem. **88**, 45 (1990); V. I. Anisimov, M. A. Korotin, and E. Z. Kurmaev, J. Phys. Condens. Matter **2**, 3973 (1990); M. Takahashi and J. Kanamori, J. Phys. Soc. Jpn. **60**, 3154 (1991).

[7] P. Kuiper, G. Kruizinga, J. Ghijsen, G. A. Sawatzky, and H. Verweij, Phys. Rev. Lett. **62**, 221 (1989); M. Abbate, F. M. F. de Groot, J. C. Fuggle, A. Fujimori, Y. Tokura, Y. Fujishima, O. Strebel, M. Domke, G. Kaindl, J. van Elp, B. T. Thole, G. A. Sawatzky, M. Sacchi, and N. Tsuda, Phys. Rev. B **44**, 5419 (1991); J. van Elp, B. G. Searle, G. A. Sawatzky, and M. Sacchi, Solid State Commun. **80**, 67 (1991).

[8] J. van Elp, H. Eskes, P. Kuiper, and G. A. Sawatzky, Phys. Rev. B **45**, 1612 (1992); D. D. Sarma, J. Solid State Chem. **88**, 45 (1990).

[9] M. Oku, H. Tokuda, and K. Hirokawa, J. Electron Spectrosc. Relat. Phenom. **53**, 201 (1991).

[10] J. Meng, P. Jena, and J. M. Vail, J. Phys. Condens. Matter **2**, 10 371 (1990).

[11] G. Dutta, A. Manthiram, J. B. Goodenough, and J.-C. Grenier, J. Solid State Chem. **96**, 123 (1992).

[12] J. R. Dahn, U. von Sacken, and C. A. Michal, Solid State Ion. **44**, 87 (1990); J. R. Dahn, U. Von Sacken, M. W. Juzkow, and H. Al-Janaby, J. Electrochem. Soc. **138**, 2207 (1991).

[13] G. Campet, B. Morel, M. Bourrel, J. M. Chabagno, D. Ferry,

R. Garie, C. Quet, C. Geoffroy, J. J. Videau, J. Portier, C. Delmas, and J. Salardenne, Mater. Sci. Eng. B **8**, 303 (1991).

[14] R. J. Hill and C. J. Howard, Program for Rietveld Analysis of Fixed Wavelength X-Ray and Neutron Powder Diffraction Patterns, Version LHPM 1, AAEC (Lucas Heights Research Laboratories, N.S.W., Australia).

[15] See, for example, B. E. Warren, X-Ray Diffraction (Addison-Wesley, Reading, MA, 1969), Chap. 13.

[16] D. E. Cox (private communication).

[17] A. J. Berlinsky, W. G. Unruh, W. R. McKinnon, and R. R. Hearing, Solid State Commun. **31**, 135 (1979).

[18] J. N. Reimers, W. Li, and J. R. Dahn (unpublished).

[19] R. Delhez, E. J. Mittemeijer, Th. H. de Keijser, and H. C. F. Rozendaal, J. Phys. E **10**, 784 (1977); B. E. Warren and B. L. Averbach, J. Appl. Phys. **21**, 595 (1950).

[20] W. Yinghua, J. Appl. Cryst. **20**, 258 (1987).

[21] G. Friedel, Compt. rend. **169**, 1147 (1919).

[22] V. A. Drits and C. Tchoubar, *X-ray Diffraction by Disordered Lamellar Structures* (Springer-Verlag, Berlin, 1991).